Inverse parameter identification of n-segmented multilinear cohesive laws using parametric finite element modeling

Mosbjerg Jensen, Simon; Martos, M. J.; Lindgaard, Esben; Bak, Brian Lau Verndal

Published in:
Composite Structures

DOI (link to publication from Publisher):
10.1016/j.compstruct.2019.111074

Publication date:
2019

Document Version
Accepted author manuscript, peer reviewed version

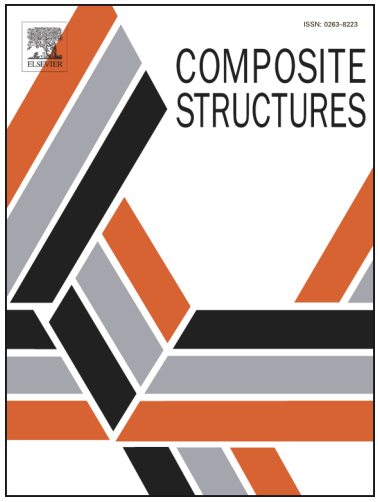

Inverse Parameter Identification of n-segmented Multilinear Cohesive Laws Using Parametric Finite Element Modeling

S.M. Jensen, M.J. Martos, E. Lindgaard, B.L.V. Bak

PII: S0263-8223(18)34618-X
DOI: https://doi.org/10.1016/j.compstruct.2019.111074
Article Number: 111074
Reference: COST 111074

To appear in: *Composite Structures*

Received Date: 20 December 2018
Accepted Date: 28 May 2019

Please cite this article as: Jensen, S.M., Martos, M.J., Lindgaard, E., Bak, B.L.V., Inverse Parameter Identification of n-segmented Multilinear Cohesive Laws Using Parametric Finite Element Modeling, *Composite Structures* (2019), doi: https://doi.org/10.1016/j.compstruct.2019.111074

s

Inverse Parameter Identification of n-segmented Multilinear Cohesive Laws Using Parametric Finite Element Modeling

S.M. Jensen[a,*], M.J. Martos[a], E. Lindgaard[a], B.L.V. Bak[a]

[a]*Department of Materials and Production, Aalborg University, Fibigerstræde 16, Aalborg DK-9220, Denmark*

Abstract

Delamination in laminated composites are efficiently modelled with the cohesive zone model (CZM). The shape of the cohesive law becomes important when simulating delamination in material systems experiencing large scale fiber bridging, as several competing damage mechanisms occurs in the fracture process zone at multiple length scales. For this purpose a multilinear cohesive law has recently been developed in [1], which readily can be adapted to a variety of shapes. However, a key challenge in applying such cohesive laws is their model calibration, i.e. identification of parameters that define the shape of the cohesive law. In this work, a new methodology for experimental characterization of multilinear cohesive laws is proposed. The methodology is an inverse approach, which identifies cohesive laws by iteratively varying cohesive zone parameters using a gradient-based optimization scheme to minimize the error in structural response between a fracture mechanical experiment and a parametric finite element model. The method is demonstrated on a moment loaded double cantilever beam (DCB) specimen made of unidirectional glass-epoxy showing large-scale fiber bridging. Multilinear cohesive laws are characterized which result in an excellent agreement between the finite element simulation and the experiment. The results and sensitivity studies demonstrate the accuracy and robustness of the proposed methodology, even for a large number of design variables in the optimization problem.

Keywords: Delamination, large scale bridging, experimental characterization of cohesive laws, inverse finite element modelling, gradient-based optimization

1. Introduction

For fibrous laminated composite structures, such as wind turbine blades, one of the most severe damage mechanisms is delamination, which is considered as a crack propagating in the interface between plies. Many fibrous laminated composites have significant R-curve behaviour due to large scale fiber bridging [1–6], i.e. the bridging length becomes comparable to or exceeds a relevant specimen dimension. This means that the cohesive zone model (CZM) approach first described in [7, 8] is well suited and therefore more often used instead of approaches based on linear elastic fracture mechanics (LEFM). Cohesive zone models assume a traction field on the crack faces close to the crack tip which acts to keep the crack faces together. In order to propagate the crack, these tractions need to be overcome by an outer applied load. The behaviour of these cohesive forces is described by a constitutive relation between interfacial tractions and interfacial separations. This relation is also referred to as the cohesive zone (CZ) law. A consequence of modelling crack propagation using CZM is that the problem becomes nonlinear, which means that all practical use of CZM involves numerical solution procedures such as the finite element method (FEM). The CZ law is defined by a set of CZ variables which control the shape of the law. Experimental characterization of the CZ variables is a central issue in applying CZM, which motivates the present work.

The experimental approaches in the open literature for characterization of CZ laws can be divided into three major categories, as briefly discussed here. The first one is a pragmatic approach which seeks simple CZ laws to represent the most essential physical properties acquired from conventional fracture mechanical tests and strength tests. Take the bilinear CZ law [9, 10] as example, which is completely defined from two independent CZ variables: The critical energy release rate and the bulk strength of the material, which individually have a sound physical interpretation. The second approach is commonly referred to as a direct method [11] or the J-integral approach. This approach relies on closed-form solutions of the path independent J-integral [12] and experimental measurements of the crack end-opening displacement δ^* [2, 13–15]. The third approach is an iterative/inverse procedure and relies on inverse parametric modelling typically using the finite element method (FEM). This approach compares numerical (or sometimes analytical [16]) solutions and experimental measurements to characterize the CZ law by iteratively varying CZ variables until the simulation and the experiment agree best possible [10, 17–25]. This is typically done using optimization techniques, i.e. minimization of the error between experimental and simulated responses. The inverse approach is computationally more intensive than the direct method. In practice, the direct method utilizes curve fitting, data smoothing, and numerical differentiation operations to derive the CZ law from the J-δ^* curve. It is well-known

Preprint submitted to Engineering Fracture Mechanics *January 10, 2019*

example, adhesive failure tests are performed on steel specimens joined by an adhesive layer in [25]. Therein, the CZ law is identified by minimization of a multi-objective problem, which includes a global load-displacement response curve and DIC measurements of the specimen's displacement field in a suitable region of interest (ROI) enclosing the crack tip. Alternatively, Ref. [24] proposed an identification procedure which rely on minimization of an error function in terms of global reaction forces in combination with distributed strain measurements along the delamination path using embedded fiber Bragg grating (FBG) sensors. The recent progress of full-field techniques motivates the sensitivity study in [27] concerning the identification of CZ laws using local full-field kinematic data. Therein, an objective function is defined as the residual between simulated and pseudo-experimental surface displacements over a ROI near the crack tip of a DCB specimen. The sensitivity of the objective function associated with the cohesive zone parameters and the displacement sampling in time (i.e. measuring instants/loading steps) and space (i.e. the size of ROI) are assessed. The results show, that the local full-field kinematic data is primarily dependent on the cohesive energy and the cohesive strength, while the effect of the traction-separation shape appears not to be significant. Nevertheless, a significant dependence of the shape of the traction-separation law is found in the case of large scale fiber bridging [1, 2, 28].

Most of the previous work on inverse parameter identification of CZ laws involve characterization of simple traction-separation relations, e.g. bilinear, trapezoidal and exponential [10, 11, 17, 27]. The parametrization of such CZ laws is straightforward and requires only a few design variables in the optimization problem, e.g. the onset traction and the critical energy release rate. However, in the event of large-scale bridging, none of these simple CZ laws can describe the crack process accurately. This calls for more advanced CZ laws [1, 2, 28]. The advanced CZ laws may be restrictive or free in shape. The shape-restricted CZ laws impose a priori assumptions on the shape of the CZ law, e.g. a trilinear CZ law [15, 18, 29] or an exponential bridging traction profile [24]. These CZ laws typically possess a relatively low number of calibration parameters, but require a priori knowledge about the material system and governing failure mechanisms at hand. For instance, mode I delamination in cross-ply carbon fiber epoxy laminates is studied in [24], wherein an exponential decay function with just three calibration parameters is adopted to describe the bridging tractions. Other advanced CZ laws are free in shape, that is, they require little/no a priori assumptions regarding their shape. Examples include multilinear CZ laws [1, 19–21] and cubic spline CZ laws [21, 22, 25]. In previous work by the authors [1] a bi-, tri-, and general mixed-mode multilinear CZ law with 15 linear segments are used to simulate delamination in a fibrous glass-epoxy DCB specimen. It is shown that adding more line segments to the CZ law, improves how accurately the R-curve effects are predicted. This is a natural consequence of more degrees of freedom in the traction-separation relation, which makes the multilinear CZ law versatile. However, the versatility of such CZ laws comes at the expense of an increased number of design variables and complexity of the optimization problem in the inverse parameter identification procedure.

To the authors' knowledge, just a handful of attempts have been conducted on characterization of advanced CZ laws with zero a priori shape assumptions [19–22, 25]. Inverse parameter identification of such CZ laws has not previously been applied to fibre reinforced polymer matrix composites with large-scale bridging. Shen et al. [21] proposed an inverse approach for identification of linear and cubic Hermite spline-based CZ laws. The identification procedure is demonstrated in mode I fracture tests on quasi-brittle materials in [22], wherein the CZ law consists of cubic Hermit splines with a total of $\mu = 5$ control points. The control points are allowed to vary freely, which yield $2\mu - 2 = 8$ design variables in the optimization problem. The number of design variables in cubic Hermit spline-based CZ laws is reduced in the work of Xu et al. [25], by making some of the control points dependent on one another. The inverse approaches in [21, 22, 25] use a zero-order Nelder-Mead (N-M) algorithm to solve the optimization problem. The solution to the optimization problem is found to be sensitive to the initial guess. This issue is remedied in [25] by making use of a two-step procedure, such that the identification procedure seeks for a simplified CZ law at first having a lower number of calibration parameters to provide a good initial guess before continuing with a more advanced CZ law.

In the recent work by Pereira et al. [19, 20], an inverse method is applied with pure mode I and pure mode II fracture tests to determine multilinear CZ laws of bovine cortical bone. The CZ laws consist of four linear softening segments, and contain four design variables in the optimization problem. The optimization problem is solved using bisection algorithms, and is found to agree with direct approaches applied to the same problem on multiple specimens.

In this work, an inverse parameter identification procedure is proposed to characterize multilinear CZ laws of fibre reinforced polymer matrix composites with large-scale bridging. The CZ laws are free in shape and include a high number of line segments, and hence design variables, to provide sufficient degrees of freedom in the traction-separation relation to enable constitutive modelling of complex and multi-scale damage mechanisms in the fracture process zone. Given the high number of design variables, a gradient-based algorithm has successfully been applied in the inverse parameter identification procedure to solve the optimization problem. The identification procedure proves very robust and insensitive to the choice of initial guess. The identification procedure is based on error minimization in measurements of a global structural response, which is convenient due to its simplicity. Additional clip gauge measurements at the initial crack tip demonstrates that the identified CZ laws are also valid at a local level.

The paper is organized as follows. In Sec. 2, the inverse approach for identification of multilinear CZ laws is presented. A brief summary of the multilinear CZ law in [1] is also included. Sec. 3 presents a case study which demonstrates the proposed method for identification of general multilinear CZ laws in unidirectional glass fiber-epoxy using mode I DCB test specimens. A presentation and discussion of results follow in Sec. 4, where the topic of interest are the robustness and performance of the method, an assessment of the global and local predictive capability and further sensitivity studies.

2. Methodology

The mixed-mode multilinear CZ law developed in [1] proves accurate in FE modelling of delamination in material systems with large-scale fiber bridging as the CZ law can adapt to a variety of shapes, and eliminates conventional a priori assumptions regarding the shape of the CZ law. However, the multilinear CZ law depends on a large number of CZ variables which needs calibration prior to its usage. An efficient and reliable method for characterization of multilinear CZ laws is proposed in this work. This section explains the details of the methodology, prior to demonstrating its application in later sections.

2.1. Inverse approach for identification of multilinear cohesive laws

The work takes point of departure in the cohesive interface element formulation proposed in [1]. Therein a mixed-mode n-segmented multilinear CZ law is implemented in a cohesive interface element through a user-defined element subroutine in ANSYS Mechanical APDL for implicit FEA. The CZ law relates interfacial cohesive tractions τ_i to crack face separations Δ_i, and is formulated in the framework of damage mechanics. A damage formulation controls degradation of cohesive tractions across the cohesive zone, which depend on the crack face separation and internal variables. The CZ law is an equivalent one-dimensional formulation, and in the general case of mixed-mode crack opening, the traction-separation relation is defined in terms of the norm of the separation vector, a work conjugate traction norm, and mode interaction criteria. In case of pure mode I crack opening, mode interactions are not active, and the CZ law reduces to a traction-separation relation between the normal traction component τ_3 and the normal separation component Δ_3. An n-segmented multilinear CZ law is illustrated in Fig. 1 for pure mode I. Every i'th line segment is uniquely defined by its end-points $\delta_3^{(i-1)},\ \sigma_3^{(i-1)}$ and $\delta_3^{(i)},\ \sigma_3^{(i)}$, which constitute the CZ variables of the CZ law. Consequently, a multilinear CZ law with n line segments contains an upper bound of $2n$ CZ variables: $\delta_3^{(i)},\ \sigma_3^{(i)}$ for $i = 1, ..., n$.

The methodology is an inverse approach which simulates a physical experiment in a parametric finite element model, and determines the CZ law by minimizing a residual using mathematical programming techniques. An outline of the identification procedure is illustrated in the flowchart in Fig. 2, which will be explained in detail in the following sections. The design variable vector $\mathbf{x}$ contains CZ variables $\delta^{(i)},\ \sigma^{(i)}$ of the multilinear CZ law with a given number of line segments n. A residual vector $\mathbf{r}$ is defined from measurements of global structural responses acquired from the experiment $\mathbf{\Psi^{Exp}}$ and the parametric finite element model $\mathbf{\Psi^{Num}}$. A scalar objective function $f(\mathbf{x})$ is defined as a non-linear least squares of the residual which is minimized using a gradient-based optimization algorithm. Once the optimization algorithm converges to an optimal solution $\mathbf{x}^*$, the multilinear CZ law has been characterized. The identification procedure is build in Matlab and simulations are performed with ANSYS Mechanical.

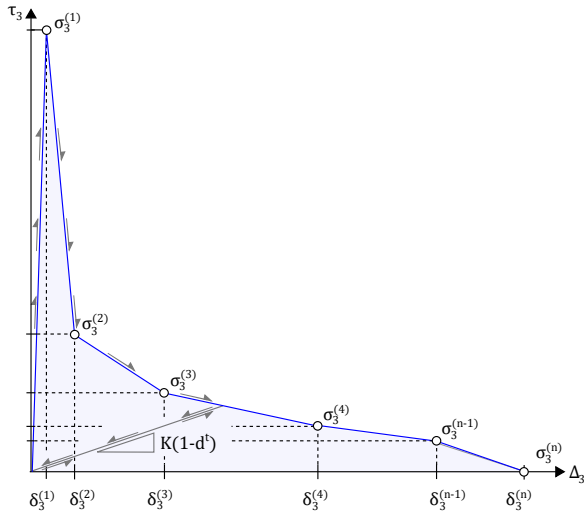

Figure 1: The n-segmented multilinear CZ law in pure mode I.

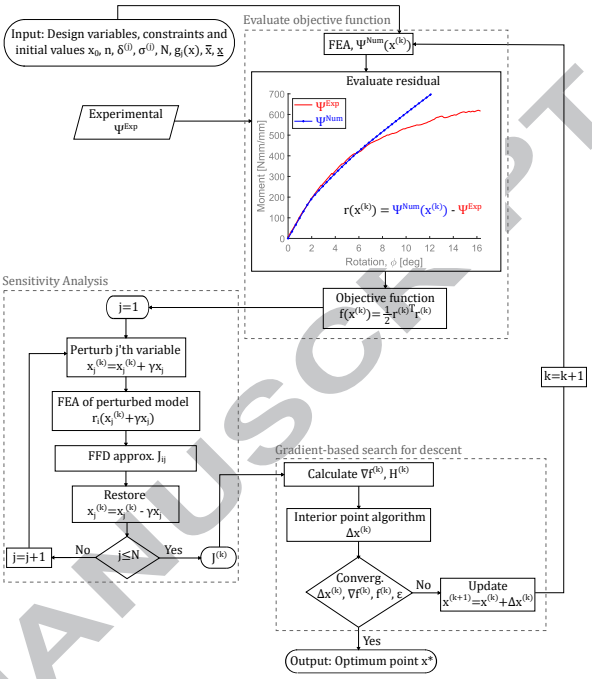

Figure 2: A flowchart for illustrating the basic concept of the procedure for identification of CZ variables.

2.2. Design variables

To start the identification procedure certain information must be provided by the user as indicated in the flowchart in Fig. 2. The identification procedure relies on a gradient-based optimization algorithm, which must be started from an initial guess $\mathbf{x_0}$. The number of design variables depend on the number of line segments n in the multilinear CZ law. The multilinear CZ law in Fig. 1 contains an upper bound of $2n$ CZ variables, however, not all CZ variables need inclusion in $\mathbf{x}$, as some CZ variables may be predefined. In this work, the separation variables $\delta_3^{(i)}$ are predefined, and only the traction variables $\sigma_3^{(i)}$ are included in $\mathbf{x}$ as design variables, see Eq. (1). Additionally, the onset traction $\sigma_3^{(1)}$ and the final traction variable $\sigma_3^{(n)}$ are excluded from $\mathbf{x}$. The former, $\sigma_3^{(1)}$, is fixed to 80% of the out-of-plane strength of the bulk material, while the latter is zero by definition. Further details on the choice of design variables are presented in Sec. 3.3. The total number of design variables will be denoted N. The current procedure for choosing design variables among the CZ variables yields a total of $N = n - 2$ design variables.

If the number of line segments is sufficiently high, predefining the separation variables in the CZ law adds little restrictions to its shape. Besides halving the number of candidate variables to be included in the optimization problem, the choice has further advantages. It is both convenient and computationally reasonable to have design variables of equal order of magnitude, units, and physical interpretation, for ease of defining constraint functions $g_j(\mathbf{x})$ and for an enhanced convergence rate [30].

$$\mathbf{x} = \begin{bmatrix} \sigma_3^{(2)} & \sigma_3^{(3)} & \sigma_3^{(4)} & \dots & \sigma_3^{(n-2)} & \sigma_3^{(n-1)} \end{bmatrix}^T \tag{1}$$

The CZ law is assumed to be softening, which is a reasonable assumption for the specimen and material system under consideration, see for example the micromechanical models of delamination in DCB specimens with cross-over fiber bridging [3]. The assumption is introduced in the optimization problem as a set of linear inequality constraints $g_j(\mathbf{x})$. The constraints ensure that the traction variables of the CZ law decrease monotonically, see Eq. 2 and Fig. 1. Furthermore, the design space is bounded by upper and lower side constraints $\bar{\mathbf{x}}$ and $\underline{\mathbf{x}}$, respectively.

$$g_j(\mathbf{x}) = x_j - x_{j-1} \leq 1 \quad \text{for} \qquad j = 2, ..., N \tag{2}$$

2.3. Objective function

The objective function is formulated as a non-linear least squares of the residual vector, see Eq. (3).

$$f(\mathbf{x}) = \frac{1}{2}\mathbf{r}^T\mathbf{r} = \frac{1}{2}\sum_{i=1}^{m} r_i^2 \tag{3}$$

The difference in measurements of the structural responses acquired from the simulation $\mathbf{\Psi^{Num}}$ and the experiment $\mathbf{\Psi^{Exp}}$ defines the residual vector $\mathbf{r}$. The structural responses under consideration in the present identification procedure, are measurements of global response curves in terms of the applied force couple M and the angle of rotation ϕ at the crack mouth of a DCB specimen. The response curves will be discussed in greater detail in later sections. For now, the residual vector is defined in Eq. (4). The integer m denotes the number of data points included in the residual vector from the response curves. The simulated response will depend on the CZ variables at the current design iterate, hence: $\mathbf{\Psi^{Num}} = \mathbf{\Psi^{Num}}(\mathbf{x})$.

$$\mathbf{r}(\mathbf{x}) = \begin{Bmatrix} \Psi_1^{Num}(\mathbf{x}) - \Psi_1^{Exp} \\ \Psi_2^{Num}(\mathbf{x}) - \Psi_2^{Exp} \\ \vdots \\ \Psi_m^{Num}(\mathbf{x}) - \Psi_m^{Exp} \end{Bmatrix} \tag{4}$$

2.4. Sensitivity analysis

The sensitivity analysis provides information to evaluate first- and second-order derivatives of the objective function, as illustrated in the flowchart in Fig. 2. The Jacobian $\mathbf{J}(\mathbf{x})$ is a $(m \times N)$ matrix, whose entry (i, j) contains the derivative of the i'th component of the residual vector r_i with respect to the j'th design variable, see Eq. (5). The derivatives of the residual are computed using a forward finite difference (FFD) method, see Eq. (5) and the j-loop in the flowchart. The parameter γx_j represents a perturbation of the j'th component of the design variable vector. The FFD method of computing the Jacobian is computationally inefficient as it needs an additional FEA for each perturbed function evaluation $\mathbf{r}(x_j + \gamma x_j)$ for all design variables $j = 1, ..., N$. Consequently, an optimization problem with N design variables requires a minimum of $N + 1$ function evaluations to evaluate the objective function and the Jacobian at the current design iterate k. The size of the perturbation is key to obtain a reasonable FFD approximation of the derivative. The error of the FFD approximation increases as the perturbation size increases, although too small perturbation size yields an imperceptible change in the residual vector. To set a proper perturbation size, a sensitivity study of the FFD approximation has been performed for a range of perturbation sizes $[10^{-1}; 10^{-8}]$. A proper perturbation size is found to be $\gamma x_j = 10^{-6}$ as this value is centrally situated in a stable region of the FFD approximation.

$$J_{ij} = \frac{\partial r_i}{\partial x_j} \approx \frac{r_i(x_j + \gamma x_j) - r_i(x_j)}{\gamma x_j} \qquad \text{for} \quad j = 1, ..., N, \quad i = 1, ...m \tag{5}$$

Despite its computational inefficiency, the FFD is very simple to implement, and the gradient computation may be done using parallel computing to speed up the FFD evaluations.

2.5. Gradient-based optimization algorithm

The gradient ∇f and Hessian $\mathbf{H} = \nabla^2 f$ of the objective function are computed according to Eq. (6) and Eq. (7), respectively [31].

$$\nabla f(\mathbf{x}) = \mathbf{J}(\mathbf{x})^T \mathbf{r}(\mathbf{x}) \tag{6}$$

$$\mathbf{H}(\mathbf{x}) = \mathbf{J}(\mathbf{x})^T \mathbf{J}(\mathbf{x}) + \sum_{i=1}^{m} r_i(\mathbf{x}) \nabla^2 r_i(\mathbf{x}) \approx \mathbf{J}(\mathbf{x})^T \mathbf{J}(\mathbf{x}) \tag{7}$$

The availability of part of the Hessian without any second-order derivatives of r_i is a distinctive feature of the least squares formulation. The Jacobian term $\mathbf{J}^T\mathbf{J}$ is often dominating over the second summation term in Eq. (7), either because the curvature of the residuals becomes negligible near the solution (that is, $\nabla^2 r_i$ are small) or because the residuals $r_i(x)$ are relatively small [31]. Consequently, a good approximation of second-order information can be obtained for nearly free once the first-order Jacobian has been computed. This useful feature of the least squares formulation has been exploited in the present work.

The optimization problem is solved using the interior-point algorithm in the Matlab optimization toolbox [32]. This algorithm enables a Hessian provided by the user and linear inequality constraints $g_j(\mathbf{x})$. Depending on the function non-convexity and Hessian rank deficiency, the interior-point algorithm switches between a quasi-Newton method in combination with a line search method, and a trust-region method with a conjugate gradient method [32]. The inverse procedure proposed, stops the optimization algorithm after the initial N+1 iterations, and restarts the optimization scheme from the current design iterate. This is done to ensure that invalid history from previous design iterates won't deteriorate the convergence. The restart is found to be efficient in later sections.

Stop criteria are formulated in terms of the design variable change $\mathbf{\Delta x}$, the objective function, and its gradients. The tolerances of the stopping criteria are problem-dependent and will be specified further in the following case study. The optimization problem is summarized in Eq. (8).

$$\begin{aligned} \text{Objective:} \quad & \min_{\mathbf{x}} f(\mathbf{x}) = \frac{1}{2} \sum_{i=1}^{m} r_i^2 \\ \text{subjected to} \quad & g_j(\mathbf{x}) = x_j - x_{j-1} \leq 1 \quad \text{for} \quad j = 2, ..., N \\ & \underline{\mathbf{x}} \leq \mathbf{x} \leq \bar{\mathbf{x}} \end{aligned} \tag{8}$$

3. Case study: Characterization of pure mode I multilinear cohesive laws

The proposed methodology is tested on a pure moment loaded DCB specimen under mode I crack opening. For that purpose, an experimental response needs to be measured, and a parametric FE model similar to that of the experiment needs to be evaluated. The experiment and the FE model is presented in the following.

3.1. Experimental results

The case study makes use of the experimental data from [5]. This section is confined to a brief outline of the experimental setup and a presentation of the experimental data. A complete description of the experiment can be found in [5]. A quasi-static delamination experiment is performed on a pure moment loaded DCB specimen in mode I crack opening. The DCB specimen is made of uni-directional glass fiber-epoxy and manufactured using the vacuum assisted resin transfer moulding process. A pre-crack is introduced during lay-up by a $13\mu m$ thick PTFE film, which is used to produce an initial sharp crack. The test specimen has a length of $L = 273.0mm$, a width of $w = 24.6mm$, and each DCB arm as a height of $h = 4.5mm$. The initial pre-crack is $a_0 = 66.0mm$ in length. Elastic material properties are as follows: Young's moduli $E_{xx} = 21.4GPa$, $E_{yy} = E_{zz} = 10.0GPa$, shear moduli $G_{xy} = G_{xz} = 4.0GPa$, $G_{yz} = 2.5GPa$, Possion's ratio $\nu_{xy} = \nu_{xz} = 0.3$, $\nu_{yz} = 0.07$. Further details on the material system can be found in [5].

A picture of the experimental setup during testing is shown in Fig. 3. Force couples are applied to the DCB specimen by a rigid connection between the DCB specimen arms and aluminium beams. The aluminium beams are part of a pulley system connected to a tensile testing machine. The angle of rotation of the aluminium beams is monitored using inclinometers, which provide a measure of the angle of rotation, ϕ, at the crack mouth of the DCB

specimen. The applied force couple, M, is measured using the load cell in the tensile testing machine. Additionally, the crack end-opening displacement, δ^*, is measured with a clip gauge positioned at the initial crack tip. Fig. 4 shows the M, δ^*-curve and the M, ϕ-curve as measured in the experiment.

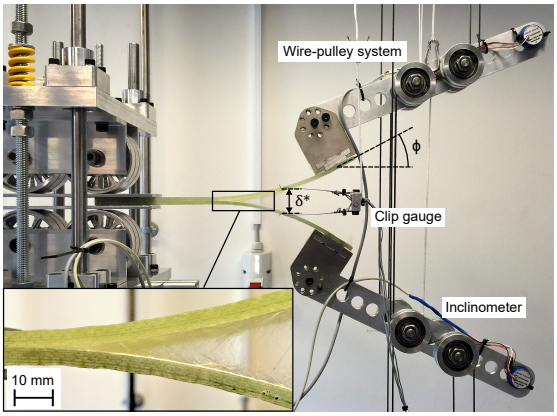

Figure 3: Experimental setup [1]. The moment is introduced to the DCB specimen through a wire-pulley system connected to a tensile test machine, which measures the applied moment through a load cell. Inclinometers measure the rotation of the DCB arms, while a clip-gauge measure the crack face separation at the initial crack tip.

Figure 4: Experimental data. Left: The applied moment M versus a local measure of the crack face separation at the initial crack tip, i.e. the end-opening separation δ^*. Right: The applied moment versus the angle of rotation Φ for the upper DCB arm.

3.2. Numerical Model

A parametric FE model similar to that of the experiment is constructed in ANSYS Mechanical APDL and used for the inverse modelling. Material properties and specimen dimensions are given in the previous section, however, the numerical model is assumed to be of unit thickness. The bulk material is modelled using eight-noded linear solid elements (SOLID185) with enhanced assumed strain to avoid shear locking. A predefined delamination path is defined at Y=0 along the interface of the DCB specimen arms. The interface is modelled with a user-defined cohesive interface element. The interface element is formulated as an eight-noded bilinear isoparametric element of zero thickness in the undeformed state. The interface element is based on the constitutive damage model and corresponding multilinear CZ law from [1], the kinematic model from [9, 33] and uses the adaptive element integration scheme described in [34], which adjust the order of quadrature depending on the element damage state.

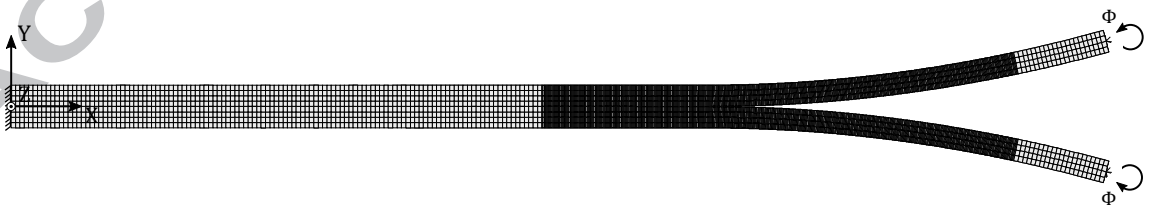

Figure 5: The finite element model of the DCB specimen in its deformed configuration. The mesh density is high in the region of expected delamination. The left end the the specimen (X=0) is clamped. The upper and lower DCB arm at the right end of the specimen (X=L) is subjected to opposite rotations around the Z-axis using multi point constraints.

The mesh of the DCB specimen is divided into a coarse mesh and a fine mesh. If crack propagation is expected in some region, a fine mesh of element dimensions 0.250 mm, 0.500 mm, 1.125 mm in the length, width, and thickness direction, respectively is used. In regions where no crack propagation is expected, a coarse mesh of dimensions 0.810

mm, 0.500 mm, 1.125 mm is used. The mesh is shown in Fig. 5 together with the imposed boundary conditions. For convenience, the applied moment load M is introduced in the FE model as prescribed rotations around the Z-axis, applied at the centre of the upper and lower DCB arms with equal magnitude and opposite signs. Since the linear solid elements do not have rotational degrees of freedom, the rotation on each DCB arm is prescribed on the entire end face as a multipoint constraint, as illustrated in Fig. 5.

The FE model is solved using a displacement-controlled Newton-Raphson iterative solver with default settings in ANSYS. A post processing macro generates an output-file which contains the simulated response curve $\mathbf{\Psi^{Num}}(\mathbf{x})$ and is readable for the identification procedure in Matlab.

3.3. Setup of the identifications procedure

The settings of the identification procedure are adjusted to the present case study. The identification procedure is solely based on global measurements of the structural response. The local validity of the identified CZ law may be verified afterwards, as will be explained in later sections. The residual vector $\mathbf{r}$ will be defined from measurements of the M, ϕ-curve. In the following, the rotation is considered to be the independent variable, and the moment to be the dependent one such that: $M, \phi \rightarrow M(\phi)$. The experimental measurements of the $M(\phi)$-curve, as shown in Fig. 4(left), determine the ϕ-range to be included in the residual $\mathbf{r}$ in Eq. (4). The $M(\phi)$-curve is recorded during formation of the fracture process zone up to and including the stage when the fracture process zone is fully developed. This allows the inverse identification procedure to characterize the complete CZ law from softening onset until final separation. The experimental measurements ($\mathbf{\Psi^{Exp}}$) of the $M(\phi)$-curve begin at the unloaded configuration of the DCB specimen ($\phi = 0$), where the crack is considered to be an initial sharp crack of length a_0. During quasi-static loading, the crack tip will advance beyond a_0 and bridging fibers will evolve in the wake of the crack tip. This increases the size of the fracture process zone until it becomes fully developed. The fracture process zone is fully developed in a pure moment loaded DCB specimen once the applied moment reaches a plateau level and stable self-similar crack propagation occurs [35]. The experimental response curve in Fig. 4 shows that the plateau is reached at approximately $\phi = 16$deg. Accordingly, $\mathbf{\Psi^{Exp}}$ will be defined by the $M(\phi)$-curve in the range $\phi \in [0; 16.3]$deg.
The residual vector includes $m = 50$ data points, such that the i'th entry denotes the error in moment $M^{(i)}$ between the simulation and the experiment at $\phi^{(i)}$ for $i = 1, ..., 50$. The ϕ-axis is divided by $m = 50$ equidistant points $\phi^{(i)}$ with a mutual spacing of $16.3\text{deg}/50 \approx 0.33\text{deg}$, as illustrated in Fig. 6. The displacement-controlled numerical model is forced to give simulation outputs at the same rotation-points $\phi^{(i)}$.

Multilinear CZ laws of varying number and distribution of line segments will be characterized in the following. At first a multilinear CZ law with $n = 15$ line segments will be characterized. The separation variables of the CZ law are predefined, as explained in Sec. 2.2, and the values are listed in Tab. 1. Several strategies can be pursued to predefine the separation variables. One strategy is to realise that the cohesive tractions are highly nonlinear with the crack opening displacements and apply additional measurements of the experimental response as a guidance to select a reasonable refinement. For the present DCB specimen and loading conditions, the applied moment squared M^2 is known to be directly proportional to the J-integral, which is related to the interfacial traction-separation relation through the partial derivative: $\sigma(\delta^*) = \partial J/\partial\delta^*$ [12, 36]. Accordingly, the M, δ^*-curve in Fig. 4 provide assisting information for predefining the separation variables. For example, the final separation $\delta_3^{(n)}$ is set equal to 9.0mm as the M, δ^*-curve reaches a plateau level in proximity to this. Application of this strategy requires that the identified CZ laws are critically assessed, e.g. elaborate on the shape of the CZ law, assess the fracture toughness, run additional sensitivity studies. An alternative strategy is to select the separation variables such that they are uniformly distributed with a fine discretization. Sensitivity studies on the number and distribution of line segments are given in a later section. The onset traction is set equal to $\sigma_3^{(1)} = 30$ MPa, which corresponds to 80% of the out-of-plane strength of the bulk material. The resulting number of design variables becomes $N = n - 2 = 13$ as listed in Tab. 1.

The optimization problem is solved with Matlab using the *fmincon* interior-point algorithm, see Sec. 2.5. Further details on the optimization options are given here. The italic text will refer to the syntax of the fmincon algorithm in the Matlab Optimization Toolbox [32]. The gradient and the Hessian of the objective function are defined by the user: *'SpecifyObjectiveGradient',true* and *'HessianFcn',@Hessian*, respectively, using Eq. (5)-(7). The stopping

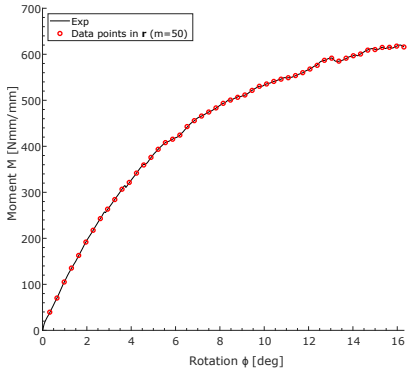

Figure 6: M(ϕ)-reseponse curve and data points included in the residual vector r.

i	1	2	3	4	5	6	7	8	9	10	11	12	13	14	15
$\delta_3^{(i)}$ [mm]	3.0E-04	0.010	0.020	0.030	0.040	0.050	0.060	0.080	0.100	0.200	0.500	1.000	3.000	5.000	9.000
$\sigma_3^{(i)}$ [MPa]	30.000	x_1	x_2	x_3	x_4	x_5	x_6	x_7	x_8	x_9	x_{10}	x_{11}	x_{12}	x_{13}	0.000

Table 1: Parameterization of the optimization problem for characterization of the 15-segmented multilinear CZ law.

tolerances are defined on the first-order optimality (*'OptimalityTolerance',1e-6*), the step size (*'StepTolerance',1e-5*), and the objective function value (*'FunctionTolerance',1e-1*). In this case study, the tolerances are tuned tight to demonstrate robustness and accuracy of the methodology. The step size tolerance may be relaxed by two to three orders of magnitude to gain speed which will be demonstrated in the following results.

4. Results and discussion

4.1. Robustness and accuracy

It is the general opinion in the open literature of inverse parameter identification of CZ laws, that the inverse problems are ill-posed and therefore solutions are usually not uniquely guaranteed [21, 22, 25]. From an optimization perspective, this means that there may exist multiple local minima in the feasible domain. In the literature, the majority of approaches utilize derivative-free optimization algorithms, e.g. the Nelder-Mead algorithm [21, 22, 25], genetic algorithms [18] and search strategies using bisection methods [19, 20]. Although the derivative-free search algorithms are simple to implement and avoid evaluation of gradients, they are not suited for problems with many design variables and they often have poor convergence rates. In this work, the optimization problem is solved using a gradient-based algorithm. To assess the robustness of the identification procedure and issues related to local minima and convexity of the optimization problem, the identification procedure is started from multiple initial guesses, i.e. shapes of the multilinear CZ law. Five different initial guesses, IG, are tested as depicted in Fig. 7 by IG1 through IG5. It is noted that the CZ laws are split into two parts of different coordinate axes for illustration purposes. The parts also represent two regions in the fracture process zone with distinctive governing damage phenomena. For short opening displacements (i.e. the left part of the CZ law in Fig. 7 where $0 \leq \delta_3 \leq 0.15$), the CZ law represents the constitutive behaviour in the near crack tip region of the fracture process zone. For larger opening displacements and lower cohesive tractions (i.e. the right part of the CZ law in Fig. 7 where $0.15 \leq \delta_3 \leq 9$), the CZ law represents the constitutive behaviour in the wake of the crack tip, which is governed by fiber bridging. The initial guesses under consideration exhibit different characteristics in these regions, which make them suitable for testing the robustness of the identification procedure. The structural responses associated with the initial guesses are shown in Fig. 8.

The identification procedure progresses with the settings described in Sec. 3.3 and converges to the CZ laws shown in Fig. 9. Details of the CZ laws are listed in Tab. 11 along with their corresponding fracture toughness

G_c. A high number of decimals are deliberately included to emphasize the uniqueness of the obtained solutions. The identification procedure converges to nearly identical and physically consistent CZ laws from the different initial guesses. The scatter in the computed CZ variables are on the order of $\pm 0.1 MPa$, which is largest in magnitude for design variables in the near crack tip region. Consequently, the gradient-based optimization procedure proves robust and insensitive to the choice of initial guesses. The simulated structural responses associated with the CZ laws in Fig. 9 are presented in Fig. 10. The simulations and the experimental data are in excellent agreement, which show that the present identification procedure is also accurate in predicting global structural responses.

4.2. Optimization history

Further information of the optimization history are shown in Fig. 12 and Fig. 13. Results are shown for initial guess IG3, however, the findings demonstrate general tendencies for all initial guesses. Fig. 12 shows the optimization history. A zoom-in is provided due to the different orders of magnitude of the objective function as the optimization algorithm progresses. A rapid decrease in the objective function occurs within the first four iterations. The associated evolution in structural response is shown in Fig. 13. The objective function decreases three orders of magnitude, and after just four iterations a reasonable overall representation of the experimental data is obtained. After completion of the 14'th ($= N + 1$) iteration, the optimization algorithm is restarted at the current design iterate. The efficiency of restarting the optimization algorithm is clearly seen by the drop in objective function in the subsequent iteration. In the remaining iterations the optimization algorithms oscillate around the minimum point until one of the stopping tolerances are met. The total number of iterations to convergence, *nIter*, for the current stopping tolerances are given in the last column of Tab. 11. The relatively high number of iterations to convergence are a consequence of the tight stopping tolerances as discussed in Sec. 3.3. However, a satisfactory solution may be obtained in less iterations if the stopping tolerances are relaxed. Fig. 14 shows that there are no notable difference in the CZ laws at *nIter*=25 and *nIter*=80 for IG3. Nevertheless, the former requires a significantly lower number of function evaluations. Consequently, the identification procedure may be tuned for both robustness and speed while handling a large number of design variables.

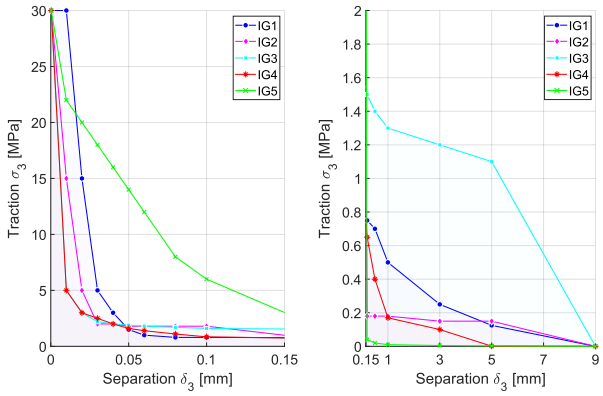

Figure 7: Five initial guesses, IG1-5, of 15-segmented multilinear CZ laws.

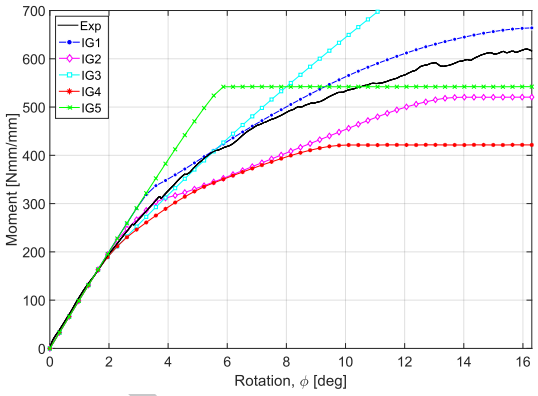

Figure 8: The structural response associated with the initial guesses IG1-5.

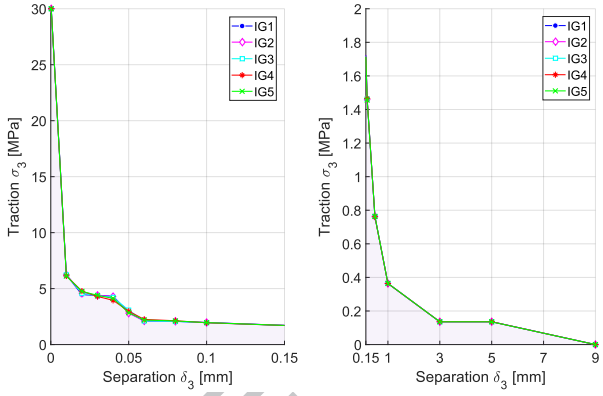

Figure 9: The identification procedure converges to nearly identical solution from IG1-5.

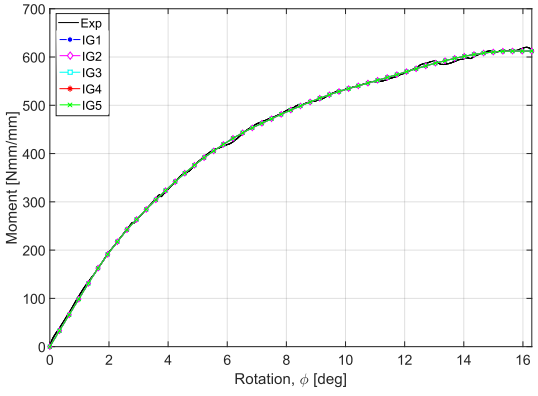

Figure 10: The structural response of the converged solutions coincides and agree well with the experiment.

	σ_3^2	σ_3^3	σ_3^4	σ_3^5	σ_3^6	σ_3^7	σ_3^8	σ_3^9	σ_3^{10}	σ_3^{11}	σ_3^{12}	σ_3^{13}	σ_3^{14}	G_c	$f(\mathbf{x}_{\mathbf{end}})$	nIter
IG1	6.237	4.549	4.389	4.323	2.863	2.103	2.078	1.969	1.464	0.761	0.364	0.136	0.136	2.294	267.43	99
IG2	6.246	4.583	4.397	4.285	2.803	2.117	2.081	1.972	1.459	0.764	0.364	0.136	0.136	2.294	267.46	80
IG3	6.230	4.568	4.357	4.215	3.079	2.106	2.064	1.956	1.463	0.763	0.364	0.136	0.136	2.295	267.48	80
IG4	6.141	4.775	4.298	3.956	2.976	2.248	2.128	1.949	1.465	0.761	0.364	0.136	0.136	2.295	267.58	79
IG5	6.116	4.756	4.399	4.126	2.846	2.192	2.111	1.963	1.456	0.763	0.364	0.136	0.136	2.294	267.55	76
AVG	6.194	4.646	4.368	4.181	2.913	2.153	2.092	1.962	1.461	0.762	0.364	0.136	0.136	2.295		

Figure 11: Numerical values of the design variables associated with 15-segmented CZ laws of the converged solutions for initial guess IG1 through IG5. Tractions are given in MPa and the critical energy release rate G_c are given in kJ/m^2. Note, the number of iterations *nIter* can be reduced significantly by relaxing the stopping tolerances of the optimization algorithm, see Sec. 4.2.

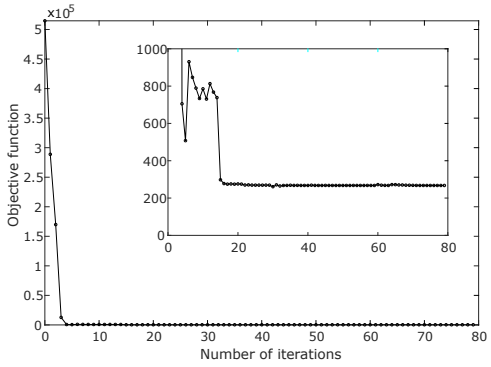

Figure 12: Optimization history for IG3. A zoom-in is provided due to the different orders of magnitude.

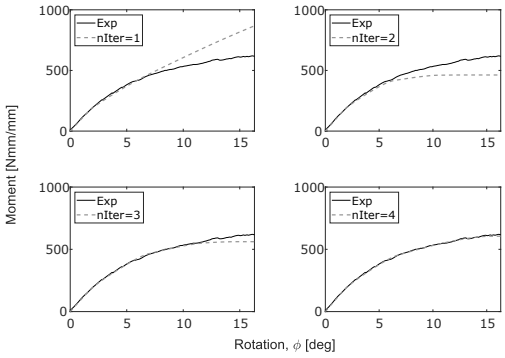

Figure 13: Progression in structural response starting from initial guess IG3. *nIter* denotes the iteration number.

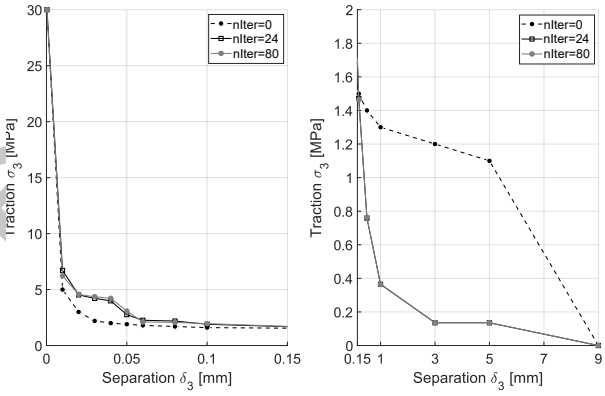

Figure 14: Progression of CZ laws IG3 for varying iteration number *nIter*.

4.3. Sensitivity to the number and the distribution of line segments

The line segments of the identified CZ laws in Fig. 9 are non-uniformly distributed according to the predefined separation variables in Tab. 1. The number and distribution of line segments of the multilinear CZ law are essential settings of the present methodology. The effect of these settings is investigated here by changing the values of the predefined separation variables $\delta_3^{(i)}$. In the present study, the separation variables are distributed as illustrated in Fig. 15 by the location of the marker symbols along the δ_3-axis. The number of line segments n under consideration are listed in Tab. 2. Apart from the number and the distribution of the line segments, the identification procedure has been started with the same settings as previously described. Fig. 15 shows the CZ laws computed by the identification procedure. Their capability to simulate the experiment is shown in Fig. 16. Clearly, the bilinear CZ law ($n = 2$) does not simulate

n	2	3	7	10	15a	15b	50
$f(\mathbf{x}_{\mathbf{end}})$	85120	5776.8	281.59	388.82	267.43	184.62	199.55
G_c $[kJ/m^2]$	1.800	2.366	2.300	2.286	2.294	2.319	2.332

Table 2: Values of the objective function and fracture toughness for the CZ laws and structural responses in Fig. 15 and Fig. 16.

the experiment adequately, due to its lacking ability to account for bridging tractions in the wake of the crack tip. Adding one line segment creates a trilinear CZ law ($n = 3$), which enables simple R-curve modelling. However, the trilinear CZ law simulates the experiment with poor accuracy, see e.g. the non-physical kink in the simulated structural response at $\phi = 3.8$deg. The 7-, 10-, and 15-segmented CZ laws appear to simulate the experiment with excellent agreement in Fig. 16. Further information on the values of the objective function and the fracture toughness of the respective CZ laws are included in Tab. 2. Although there are no notable difference in the response curves in Fig. 16 for the 7-, 10-, and 15-segmented multilinear CZ laws, there are differences in the values of the associated objective function.

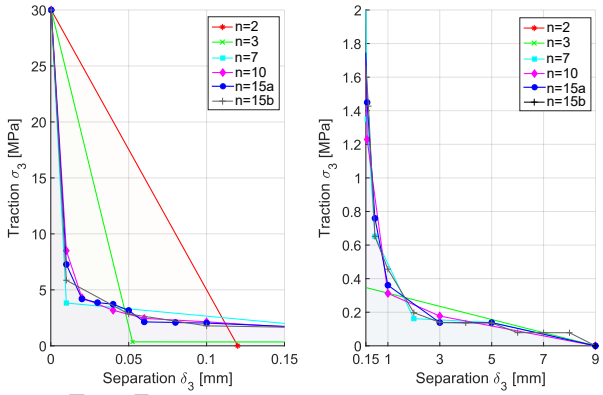

Figure 15: Structural response in terms of moment versus angle of rotation for CZ laws of varying number of line segments n.

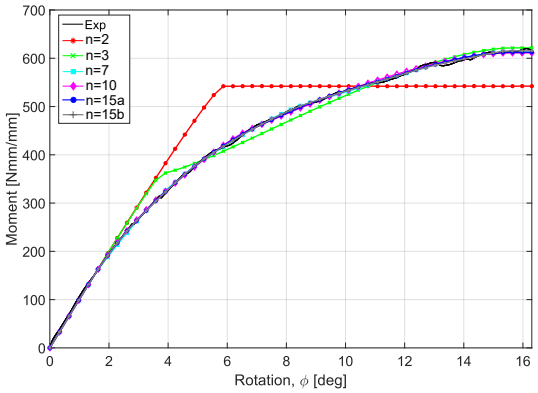

Figure 16: Structural response in terms of moment versus angle of rotation for CZ laws of varying number of line segments n.

The objective function value does not decrease monotonically with increasing number of line segments because the distribution of the line segments are different. For instance, the 7-segmented CZ law attains a lower objective function value than the 10-segmented CZ law, despite the higher number of line segments in the latter. The influence of the distribution of the line segments becomes more clear by comparison of the 15a and 15b multilinear CZ laws. Despite the common total of 15 linear segments, the former has more linear segments in the left part of Fig. 15, while the latter contains more line segments in the right part of Fig. 15. The considerably lower value of the error function associated with 15b is due to the more degrees of freedom in the traction-separation relation to describe the bridging tractions, which governs the delamination process. The significance of the bridging tractions over the cohesive tractions in the close vicinity of the crack tip is due to the difference in length scale and the associated fracture energy

uptake of the two regions within the fracture process zone.

Accordingly, both the number of line segments and their distribution influence the error between the simulated and experimental response curves. The results in Fig. 15 and Tab. 2 show that the present methodology identifies CZ laws which are consistent in shape and fracture toughness. The separation values of the multilinear CZ law may also be uniformly distributed. The methodology has been applied to identify a multilinear CZ law with 50 line segments and equidistant separation variables. The resulting CZ law is shown in Fig. 20 along with the 15b multilinear CZ law, which is seen to be consistent in shape.

4.4. Local response and validity

The experiment and the numerical model is compared in terms of an additional measure of the structural response, which is neither global nor included in the objective function of the optimization problem as opposed to the $M(\phi)$-response curve. The purpose of this comparison is twofold: Firstly, to assess the ability of the multilinear CZ law as obtained with the inverse approach to simulate an independent experimental response that is not explicitly included in the objective function. Secondly, to elaborate on the local validity of the identified CZ law.

The local experimental response under consideration is the applied J-integral versus the end-opening displacement. In the experiment, the end opening displacement δ^* is measured by a clip gauge attached on pins mounted at the location of the initial crack tip of the DCB specimen, as illustrated in Fig. 18. A closed-form solution of the applied J-integral for a DCB specimen subjected to pure bending is available in [37], wherein it is shown that the path independent J-integral is directly proportional to the applied moment squared: $J = (12M^2)/(wh^3E_{xx})$, which applies in case of large scale fiber bridging [5, 37], here assuming orthotropic material and plane stress conditions. The resulting experimental response curve is shown in Fig. 17, which has been derived from the closed-form solution of the J-integral, and the experimental measures of the applied moment M and the crack end-opening displacement as graphed in Fig. 4. A similar response is extracted from the numerical model using cohesive elements with the multilinear CZ law denoted 15a and 15b in the previous section, see Fig. 15. The simulated response curves are included in Fig. 17. The squaring of M magnifies discrepancies between the two response curves, nevertheless, a good agreement between the experiment and the simulation is achieved. Since the end opening displacement δ^* is a measure of the local response at the initial crack tip, the results in Fig. 17 also show that the identified multilinear CZ laws are valid at a local level.

In the numerical model, the crack face separation is measured exactly at the initial crack tip, however, in reality the location of the clip gauge pins may be offset with respect to the exact crack tip position. Therefore, two additional simulated response curves are included in Fig. 17 to represent an upper and lower bound of uncertainty due to systematic errors in locating the clip gauge pins at the initial crack tip. The additional response curves are obtained by post-processing the FE simulation with ±1mm offset in the clip gauge pin location along the specimen's length direction. The results in Fig. 17 show that the uncertainty of locating the clip gauge pins exactly at the initial crack tip, can have a considerable influence which in some cases is large enough to explain the discrepancy between the experimental and simulated local responses.

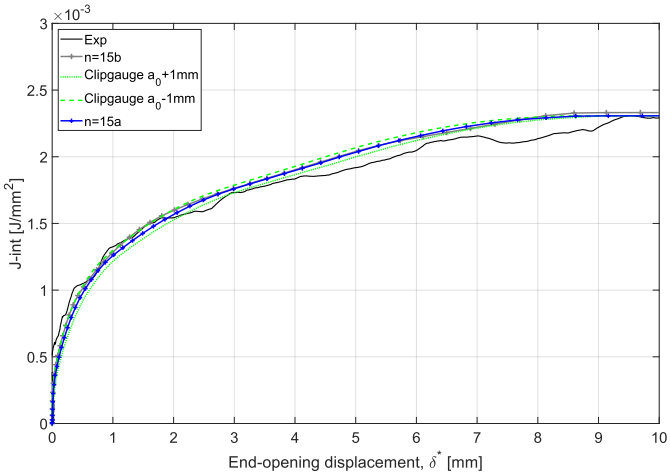

Figure 17: Simulated and experimentally measured J-integral versus the crack opening displacement at the initial crack tip. The simulated response is obtained using the 15a- and 15b segmented multilinear CZ law. A sensitivity study of the clip gauge pin locations is also included (using the the 15a multilinear CZ law.

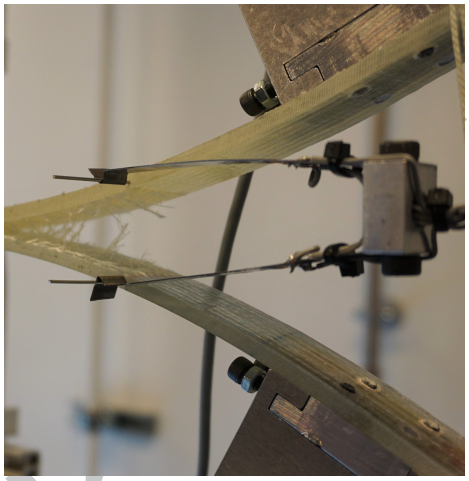

Figure 18: A detailed view of the clip gauge and clip gauge pins for measuring the end opening displacement δ^* (the image is not taken during testing but made for illustration purposes only).

The CZ law may also be derived using a direct method. The direct method rely on calculating the J-integral, and differentiating it with respect to the end-opening displacement to determine the CZ law: $\sigma(\delta^*) = \partial J/\partial\delta^*$ [2, 12, 35]. For completeness, a comparison is added in Fig. 20, which show the multilinear CZ law identified with the inverse approach and CZ laws derived from a direct method. The authors acknowledge that there are several approaches in the open literature to perform data fitting and numerical differentiation in deriving the CZ laws with direct methods e.g. [36, 38]. Here the derivative of the J-integral with respect to the end-opening displacement is determined for all data points in Fig. 17 by fitting a linear function to every data point within a moving fitting window which is centred around the data point of interest as illustrated in Fig. 19. The CZ laws derived using the direct approach is shown in Fig. 20 for three different settings of the fitting window. Increasing the size of the fitting window increase the level of data smoothening. The asymptotic behaviour of the CZ law and the fluctuation in the J, δ^*-curve give rise to non-physical repeated intersections with the first axis, which makes it difficult to determine the value of the critical opening separation $\delta^{(n)}$ where the cohesive traction are zero. This may be avoided by processing the raw experimental data prior to numerical differentiation, e.g. by data smoothening or curve fitting, however, in that case, the resulting CZ laws will be sensitive to the choice of curve fitting or smoothening operations [26]. As the direct method rely on local measures of the crack opening displacement, the resulting CZ law will also be sensitive to the accurate definition of the crack tip or clip gauge locations as illustrated in the sensitivity study of $a_0 \pm 1$mm in Fig. 17.

In these aspects, an inverse approach based on global measurements of the structural response is simple, and the approach is seen to identify multilinear CZ laws which enables one to simulate local measurements of the structural response in agreement with the experiment.

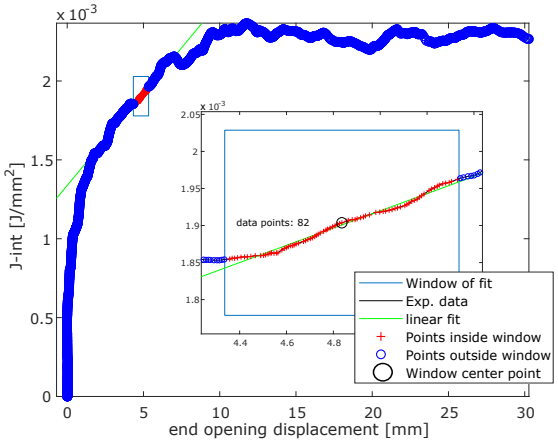

Figure 19: The derivative of the J-integral w.r.t. the end-opening displacement is computed by fitting a linear function to every data point within a moving fitting window.

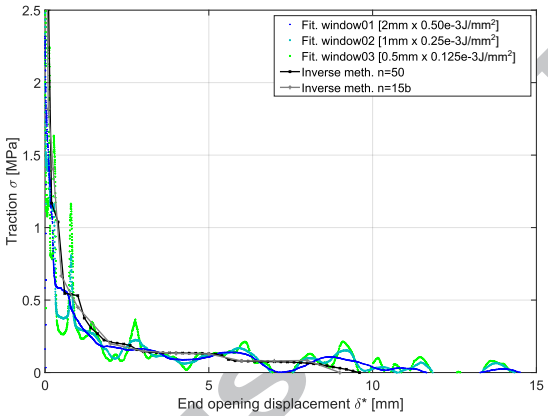

Figure 20: Comparison of CZ laws derived from Fig. 17 by a direct method and the multilinear CZ laws (n=15b and n=50) as obtained with the inverse method based on a global structural response.

5. Conclusion

Multilinear CZ laws are particularly suited to model delamination with large scale bridging, as these eliminate a priori shape assumptions, and posses sufficient degrees of freedom in the traction-separation relation to model the constitutive behaviour of complex and multi-scale fracture processes. A key challenge in applying advanced CZ laws is their model calibration, i.e. identification of CZ variables, due to the increased size and complexity of the problem. In this work, a robust and accurate methodology is proposed for identification of CZ variables of a multilinear CZ law as proposed in [1]. The methodology is an inverse approach, which identifies CZ variables by parametric finite element modelling and gradient-based optimization to minimize the error in structural response between an experiment and the simulation. The identification is based on global structural response curves, but the validity at local level is verified from measurements of the crack face separation at the initial crack tip. The identification procedure proves very robust in obtaining identical and physically consistent solutions with excellent predictive capabilities. The identification procedure is also shown to be insensitive to the initial guess, and converge to shape-consistent CZ laws for different user-defined settings of the methodology.

References

[1] S. Jensen, M. Martos, B. Bak, E. Lindgaard, Formulation of a mixed-mode multilinear cohesive zone law in an interface finite element for modelling delamination with r-curve effects, Submitted to Composite Structures (*under review*).
[2] B. F. Sørensen, T. K. Jacobsen, Large-scale bridging in composites: R-curve and bridging laws, Composites Part A (29A) (1998) 1443–1451.
[3] S. M. Spearing, A. G. Evans, The role of fiber bridging in the delamination resistance of fiber-reinforced composites, Acta metall. mater. 40 (9) (1992) 2191–2199.
[4] L. Sorensen, J. Botsis, T. Gmür, J. Cugnoni, Delamination detection and characterisation of bridging tractions using long fbg optical sensors, Composites: Part A 38 (2007) 2087–2096.
[5] E. Lindgaard, B. L. V. Bak, Experimental characterization of delamination in off-axis gfrp laminates during mode i loading, Composite Structures (*In press*)doi:10.1016/j.compstruct.2019.04.022.
[6] L. Canal, M. Alfano, J. Botsis, A multi-scale based cohesive zone model for the analysis of thickness scaling effect in fiber bridging, Composites Science and Technology 139 (2017) 90–98.
[7] G. I. Barenblatt, The mathematical theory of equilibrium cracks in brittle fracture, Journal of Advance Applied Mechanics 7 (1962) 55–129.
[8] D. S. Dugdale, Yielding of steel sheets containing slits, Journal of the Mechanics and Physics of Solids 8 (2) (1960) 100–104.
[9] A. Turon, P. Camanho, J. Costa, C. Davila, A damage model for the simulation of delamination in advanced composite under variable-mode loading, Mechanics of Materials 38 (2006) 1072–1089.
[10] L. Bouhala, A. Makradi, S. Belouettar, A. Younes, S. Natarajan, An xfem/czm based inverse method for identification of composite failure parameters, Computers and Structures 153 (2015) 91–97.

[11] S. Gowrishankar, H. Mei, M. K. Liechti, R. Huang, A comparison of direct and iterative methods for determining traction-separation relations, Int J Fract 177 (2012) 109–128.
[12] J. R. Rice, A path independent integral and the approximate analysis of strain concentration by notches and cracks, Journal of Applied Mechanics 35 (1968) 379–386.
[13] F. Leone, D. Girolamo, C. Davila, Progressive damage analysis of bonded composite joints, Tech. Rep. NASA/TM-2012-217790, NASA (2012).
[14] C. Sarrado, A. Turon, J. Costa, J. Renart, An experimental analysis of the fracture behavior of composite bonded joints in terms of cohesive laws, Composites: Part A 90 (2016) 234–242.
[15] M. Heidari-Rarani, M. M. Shokrieh, P. P. Camanho, Finite element modeling of mode i delamination growth in laminated dcb specimens with r-curve effects, Composites: Part B 45 (2013) 897–903.
[16] B. D. Manshadi, E. Farmand-Ashtiani, J. Botsis, A. P. Vassilopoulos, An iterative analytical/experimental study of bridging in delamination of double cantilever beam specimen, Composites: Part A 61 (2014) 43–50.
[17] N. Valoroso, S. Sessa, M. Lepore, G. Cricri, Identification of mode-i cohesive parameters for bonded interfaces based on dcb test, Engineering Fracture Mechanics 104 (2013) 56–79.
[18] F. A. M. Pereira, J. J. L. Morais, M. F. S. F. de Moura, N. Dourado, M. I. R. Dias, Evaluation of bone cohesive laws using an inverse method applied to the dcb test, Engineering Fracture Mechanics 96 (2012) 724–736.
[19] F. A. M. Pereira, M. F. S. F. de Moura, N. Dourado, J. J. L. Morais, J. Xavier, M. I. R. Dias, Direct and inverse methods applied to the determination of mode i cohesive law of bovine cortical bone using the dcb test, International Journal of Solids and Structures 128 (2017) 210–220.
[20] F. A. M. Pereira, M. F. S. F. de Moura, N. Dourado, J. J. L. Morais, J. Xavier, M. I. R. Dias, Determination of mode ii cohesive law of bovine cortical bone using direct and inverse methods, International Journal of Mechanical Sciences 138-139 (2018) 448–456.
[21] B. Shen, I. Stanciulescu, G. Paulino, Inverse computation of cohesive fracture properties from displacement fields, Taylor & Francis 18 No. 8 (2010) 1103–1128.
[22] B. Shen, G. Paulino, Direct extraction of cohesive fracture properties from digital image correlation: A hybdid inverse technique, Experimental Mechanics 51 (2011) 143–163.
[23] J. Affagaard, M. F., J. Guimard, F. Hild, Identification method for the mixed mode interlaminar behavior of a thermoset composite using displacement field measurements and load data, Composites Part A 91 (2016) 238–249.
[24] E. Farmand-Ashtiani, D. Alanis, J. Cugnoni, J. Botsis, Delamination in cross-ply laminates: Identification of traction-separation relations and cohesive zone modelling, Composites Science and Technology 119 (2015) 85–92.
[25] Y. Xu, Y. Guo, L. Liang, Y. Liu, X. Wang, A unified cohesive zone model for simulating adhesive failure of composite structures and its parameter identification, Composite Structures 182 (2017) 555–565.
[26] L. Sorensen, J. Botsis, T. Gmür, L. Humbert, Bridging tractions in mode i delamination: Measurements and simulations, Composites science and technology 68 (2008) 2350 – 2358.
[27] M. Alfano, G. Lubineau, G. H. Paulino, Global sensitivity analysis in the identification of coheisve models using full-field kinematic data, International Journal of Solids and Structures.
[28] C. Dávila, C. Rose, P. Camanho, A procedure for superposing linear cohesive laws to represent multiple damage mechanisms in the fracture of composites, Int J Fract 158 (2009) 211 – 223.
[29] A. L. Hansen, E. Lund, B. F. Sørensen, Simulation of crack growth and r-curve behavior using cohesive zone modeling, unpublished (2009).
[30] J. S. Arora, Introduction to Optimum Design, 3rd Edition, Engineering Optimisation, Elsevier Inc, 2012.
[31] J. Nocedal, S. J. Wright, Numerical Optimization, 2nd Edition, Springer Science+Business Media, LLC., 2006. doi:10.1007/978-0-387-40065-5.
[32] MathWorks, Matlab - optimization toolbox user's guide, r2017b.
[33] E. Lindgaard, B. Bak, J. Glud, J. Sjølund, E. Christensen, A user programmed cohesive zone finite element for ansys mechanical, Engineering Fracture Mechanics 180 (2017) 229–239.
[34] B. L. V. Bak, E. Lindgaard, E. Lund, Analysis of the integration of cohesive elements in regard to utilization of coarse mesh in laminated composite materials, International Journal for Numerical Methods in Engineering 99(8) (2014) 566–586. doi:10.1002/nme.4688.
[35] Z. Suo, G. Bao, B. Fan, Delamination R-curve phenomena due to damage, Journal of the Mechanics and Physics of Solids 40 (1) (1992) 1–16.
[36] B. F. Sørensen, P. Kirkegaard, Determination of mixed mode cohesive laws, Engineering Fracture Mechanics 73 (2006) 2642–2661.
[37] B. F. Sørensen, K. Jørgensen, T. K. Jacobsen, R. C. & Østergaard, Dcb-specimen loaded with uneven bending moments., International Journal of Fracture 141 (1) (2006) 163–176.
[38] J. Høgberg, B. Sørensen, U. Stigh, Constitutive behaviour of mixed mode loaded adhesive layer, International Journal of Solids and Structures 44 (2008) 8335–8354.